Journal of Energy Storage 117 (2025) 116180

Contents lists available at ScienceDirect

Journal of Energy Storage

journal homepage: www.elsevier.com/locate/est

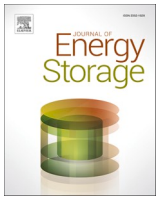

Research Papers

Deriving the numerical value of LIB mathematical model parameters from experiments: Case of as-formed and aged NMC/LMO cathodes

Francesco Tavola *, Andrea Casalegno, Gabriele Sordi, Claudio Rabissi, Benedetto Bozzini

Politecnico di Milano, Dipartimento di Energia, via Lambruschini 4, 20156 Milano, Italy

ARTICLE INFO

Keywords:
LIB
Lithium
Battery
P2D model
Parametrization
Cathode
Degradation

ABSTRACT

This study presents an experimental approach to the parameterization of lithium-ion battery cathodes for the Pseudo-Two-Dimensional (P2D) model, focusing on blended NMC532/LMO, commonly used in automotive batteries. Specifically, we are proposing an Experimental Battery Parameterization (EBP) protocol to determine key material parameters through direct measurement rather than relying on literature values. The research examines as-formed and aged cathodes, revealing significant changes in electrochemical behaviour, structural integrity, and material composition after ageing. Ageing effects, such as particle fracture, increased lithium content, and changes in porosity and conductivity, were observed. While as-formed cathodes showed higher theoretical capacities, aged ones exhibited lower activation energies for lithium diffusion, indicating enhanced ion mobility, accompanied by structural degradation. Our study emphasizes that experimental parameterization, especially in the case of aged batteries, is essential to have a precise grasp over the scope and limitations of the P2D model and identify areas for model improvement.

1. Introduction

Battery models that describe battery behaviour represent valuable tools for the design and management of batteries. In this context, physics-based models employ fundamental electrochemical and materials-science principles to describe the battery behaviour [1,2]. Sometimes electrochemical and thermal modelling are combined [3]. The physico-chemical basis can also be expanded to account for degradation phenomena [4]. Among physics-based models, the Newman pseudo-two-dimensional (P2D) model [5–7] stands out as the most widely employed one. This model offers a description of the porous electrodes and of the separator, employing a 1D geometry to describe the electrodes and separator, into which a 1D (radial) model of spherical particles within the electrode active material interval is embedded [5–9], making it in fact a lowest bulk-surface model [10]. Owing to its widespread use, P2D can be regarded as a sort of standard LIB modelling tool and the present work will refer to it. P2D is typically employed to compute electrochemical responses, such as charge/discharge and EIS, carrying out parametric analyses of the impact of variations of battery design, electrode architecture [11], operating temperature [12] and selected material parameters, mimicking batter ageing [13]. Like all PDE-based models, the solving P2D requires numerical values of a variety of parameters, many of which refer to battery materials. Of course, the predictive accuracy of the model hinges upon these parameter values, which serve as representations of battery physics, chemistry, and electrochemistry. Obviously, their accuracy is highly contingent on battery geometry, thermodynamics, and kinetics [8,14], not to mention SOH. Commonly, model-centred publications utilize parameter values obtained from the literature, without *ex professo* effort to critically examine their concrete representatively of experimental conditions. P2D battery simulation accuracy relies on a large number of physical parameters which, in the case of the widespread Doyle-Fuller-Newman model (DFN) model, can grow above 30for a full cell simulation. However, it is crucial to assess the actual impact of each parameter value on model response, in order to distinguish high-sensitivity fundamental parameters from potentially negligible ones.

A dedicated activity on this topic was conducted in our group to assess the actual impact of each parameter value on the P2D model response [12]. In this work, a thorough sensitivity analysis has been conducted on 28 different parameters, considering the impact on model response to different battery states (temperature and SOC) and electrochemical programs (discharge, relaxation and EIS).

The analysis revealed that diffusion-related parameters are the most critical ones for accurate discharge test simulation. Specifically, in the present context, these parameters are the solid diffusivity constants of

* Corresponding author.
E-mail address: francesco.tavola@polimi.it (F. Tavola).

https://doi.org/10.1016/j.est.2025.116180
Received 6 December 2024; Received in revised form 13 February 2025; Accepted 9 March 2025
Available online 14 March 2025

Nomenclature

P2D	Pseudo-two-dimensional model
LIB	Lithium-ion battery
SOH	State of health
RMSE	Root mean square error
NGM	Numerical global minima
DL	Deep learning
EBP	Experimental battery parameterization
ICP-MS	Inductively coupled plasma-mass spectrometry
SEM	Scanning electron microscopy
EDS	Energy-dispersive X-ray spectroscopy
GS	Galvanostatic polarization
EIS	Electrochemical impedance spectroscopy
GITT	Galvanostatic intermittent titration technique
NMC523-LMO	Nickel manganese cobalt oxide (523 ratio) and lithium manganese oxide
E_{TH}	Electrode thickness
D_p	Lithium-ion diffusion coefficient in the solid phase
σ_p	Electronic conductivity
R_p	Particle radius of active material grains
OCV	Open circuit voltage
k	Reaction rate constant
E_a	Activation energy
$c_{s,max}$	Maximum solid-phase lithium concentration
j_0	Exchange current density
E_W	Electrode width
E_L	Electrode length
E_{CC}	Electrode current collector thickness
ε_{AM}	Volume fraction of active material
ε_{EL}	Volume fraction of electrolyte (void fraction)
C_{dl}	Double layer capacitance
CPE	Constant phase element
IEC	International Electrotechnical Commission
SOC	State of charge
DMC	Dimethyl carbonate
NMP	N-Methyl-2-pyrrolidone
EFC	Equivalent full cycles
NT	Neutron tomography
XT	X-ray tomography
FIB	Focused ion beam imaging
ICP-OES	Inductively coupled plasma-optical emission spectrometry
CC-CV	Constant current-constant voltage charging protocol

both the electrodes, influencing lithium transport within the electrodes, and the ionic conductivity of the electrolyte, affecting the rate of lithium-ion transport through the electrolyte itself. In addition, EIS was shown to be highly sensitive to parameters related to ohmic overpotential such as kinetic rate constants and double layer capacitances of both the electrodes [12]. Solid particle radii exhibit a twofold effect, since the surface-to-volume ratio affects both the surface area for electrochemical reactions and the diffusion domain size.

Omitting the refinement of material parameter values results in loss of information regarding the peculiarities of manufacturing processes, the impact of electrode architecture - including binders and conductivity carbon and their mutual arrangements - and the specific status of the battery - that is determined by cumulative irreversible phenomena. In some cases, refinement of selected parameters is performed by minimizing the RMSE between model simulations and experimental data, typically with euristic approaches not based on the formal minimization of an objective function [15]. Moreover, with the rapid advancement of LIB technology and the introduction of novel electrode chemistries, the parameter values available in the literature become rapidly outdated or are not representative. Finally, it is necessary to account for parameter evolution with device ageing [16]. As far as the assignment of concrete numerical values to the model parameters is concerned, to the best of our knowledge, no attempts of parameter identification have been attempted with minimization tools. This situation is certainly understandable because, on the one hand the exploration of the parameter space of PDE electrochemical models with least-squares methods is indeed feasible, but it is a formidable mathematical task [17] and, on the other hand, even simple analytical electrochemical models have been shown to give rise to an infinite number of numerical global minima (NGM) [18]. The outcome of a minimum search problem would most probably lead to a local minimum, the physical meaning of which is probably questionable and, owing to the density of NGMs in the parameter space no clear guidelines are available to search a more physical local minimum. Certainly, DL-based approaches ensure a better management of the parameter identification problem for electrochemical PDE models [19]. An alternative approach is that of experimentally measuring these parameters. Of course, full experimental parameterization is a demanding and time-consuming task, requiring expertise is in the fields of battery disassembly and materials characterization. Nevertheless, this relatively rarely employed approach [15,20–24] has the potential of enhancing accuracy and enabling robust predictive capabilities. Various works in the literature propose techniques for material characterization that rely on sophisticated measurements [15] such as neutron tomography (NT) [22], X-ray tomography (XT) [23], and focused ion beam imaging (FIB) [24]. In this scenario, the objective of the present research is to formulate a simple and effective protocol for experimental battery parameterization (EBP), relying on easily accessible analytical and electroanalytical tools. Specifically, our EBP protocol is based on: (i) inductively coupled plasma-mass spectrometry (ICP-MS) for qualitative and quantitative elemental analysis; (ii) scanning electron microscopy SEM imaging, calibrated against mercury porosimeter, for porosity quantification; (iii) energy-dispersive X-ray spectroscopy (EDS) for local compositional analyses; (iv) galvanostatic polarization (GS); (v) electrochemical impedance spectrometry (EIS), and (vi) galvanostatic intermittent titration (GITT). In this work, we show that with these seven analytical methods, it is possible to estimate the totality of the P2D parameters regarding the cathode [5–7] in both as formed and aged condition. The cathodic EBP protocol yields the 19 parameters – listed in Fig. 1 –, required for the stationary and transient versions of the P2D model.

As batteries age, their parameters change over time, necessitating periodic updates to model parameterization to ensure accurate representation of the ageing process [16].

The EBP protocol can also be used to monitor battery ageing, jointly allowing both the quantification of degradation and parameterization. A detailed examination of parameter variations can further highlight the limitations of the P2D model, when it comes to describing aged batteries. In fact, the battery simulation community has concentrated on developing new models [25,26] or enhancing the features of the P2D model for thermo-electrochemical ageing simulations [27], with a focus on selecting the most degradation-sensitive parameters through fitting methods [28].

To the best of the authors' knowledge, no existing work in the literature links materials science to battery modelling, while exploring the effects of degradation on parameters.

In particular, we shall concentrate on blended NMC523-LMO blended cathodes, in as-formed and aged conditions, but the approach is general and can be straightforwardly applied to other types of cathode and anode materials. Finally, a critical discussion of the results is presented, comparing them with other parameterization protocols

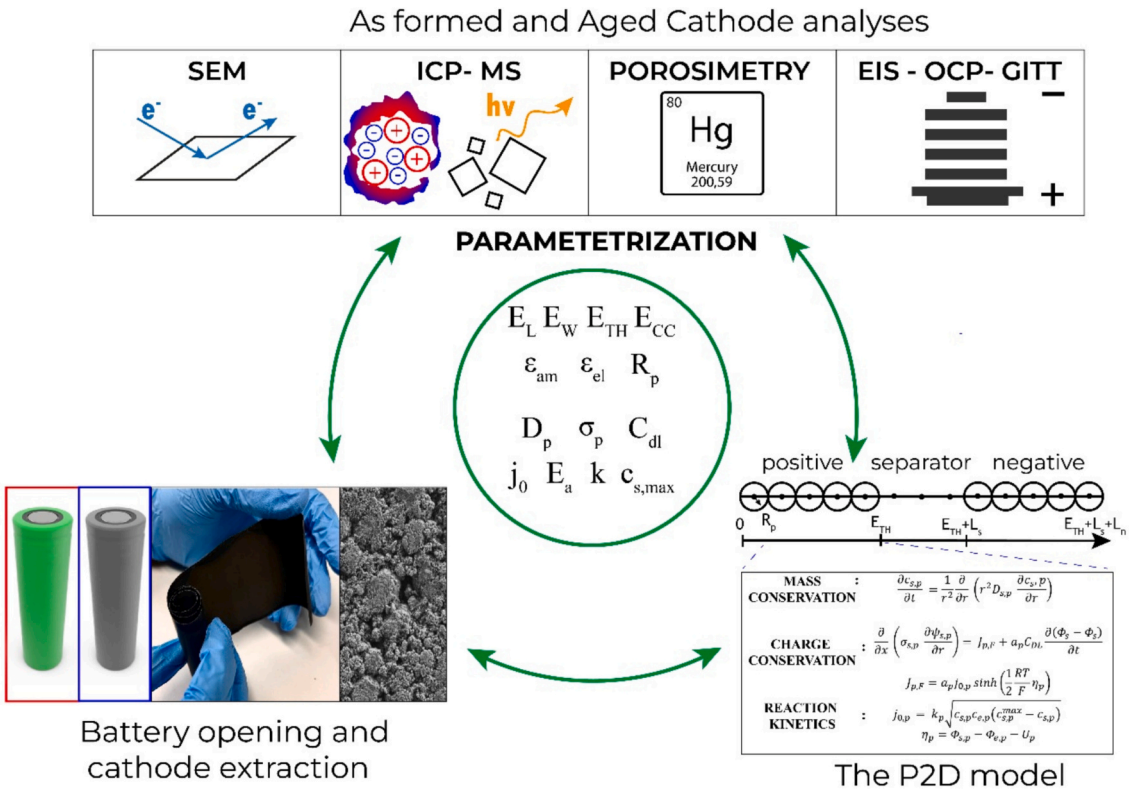

Fig. 1. Schematic of the experimental battery parameterization (EBP) protocol proposed in this work. Analytical and electroanalytical methods for the estimation of battery material observables; Estimation of P2D model parameters from battery material observables; Battery opening and material extraction for as formed and aged cathode; the cathode integration domain consisting in a 1D description of the cathode as a homogeneous porous electrode, with Li intercalation modelled by spherical diffusion with boundary conditions derived from the solution of the mass- and charge conservation problems in the porous electrode.

proposed in the literature.

2. Materials and methods

2.1. The mathematical battery model considered and its parameters

P2D models (mono 1D or three 3D dimensional) rely on partial differential equations (PDE) for the description of the cathode electrochemical behaviour: (i) charge conservation, (ii) mass conservation and (iii) electrode reaction kinetics. Fig. 1 summarizes the equations required to model the cathode and its associated parameters, as well as the experimental protocol employed to estimate the parameter values.

More specifically, the 1D P2D battery model describes a cross-section of the cathode perpendicular to the current-collector, of thickness (E_{TH}), as a material continuum, in which an appropriate number of 0 D grains of active material are placed regularly along the space coordinate x represent electrode active grains. Mass and charge conservation equations are solved in this domain, with the following material constants Li^+ diffusion coefficient D_p, electronic conductivity σ_p and ionic conductivity, that, in the LIB context, can be derived from D_p through Einstein relation.

Intercalation into the active material grains is then described by considering mass-transport in spheres of radius R_p, the boundary conditions for which are retrieved from the mass and charge conservation equations solved at the positions where the 0 D grains are placed along the x coordinate. Positive electrode solid phase lithium diffusion coefficient (D_p) controls mass-transport in the spherical cathode-material grains. In the standard P2D model, the particle geometry is described only by R_p, a possible improvement could account for the real-life polydispersity of the active-material granulometry.

Electrochemical reaction kinetics, accounting for the faradaic current, is described with the Butler-Volmer equation, that contains the following parameters: open circuit voltage (OCV), reaction rate (k), activation energy (E_a), equilibrium Li^+ concentration ($c_{s,max}$) and exchange current density (j_0).

In addition, the homogenous description of the porous electrode is obtained by assigning parameters describing the electrode geometry and architecture: electrode width (E_W) and length (E_L), current collector thickness complete the characterization and parametrization (E_{CC}), electrode volume active material fraction (ε_{AM}) – including active material, conductivity carbon and binder – and the void (ε_{EL}) fractions, accounting for the electrode porosity [8,29]. Since the P2D model considers that all voids are filled with electrolyte, it follows that $\varepsilon_{AM} = 1 - \varepsilon_{EL}$. Moreover, it is worth noting that P2D ignores other descriptors of the pore population, such as the size, shape and distribution of pores.

Finally, the time-dependent description of electrode behaviour requires the description of capacitive current, that requires the assignment of the double layer capacitance (C_{dl}). Since the real-life dynamic response of a battery is better described through a distribution of C_{dl}s, a potential improvement of the P2D model could include a CPE element rather than a mere capacitor.

For classification convenience, the above-indicated parameters can be listed under headings that emphasize their physical role, as follows.

(i) *Battery design parameters* - E_W, E_L, E_{CC}, E_{TH}, ε_{EL}, R_p describing the cell geometry at micro and macro electrode scale; (ii) *Electrode material parameters* - σ_p, D_p which appear in the mass and charge conservation equations and (iii) *Electrokinetic parameters* – describing the electrochemical reaction and double-layer charging processes occurring at the active-material grain/electrolyte interface C_{dl}, OCV, k, E_a, $c_{s,max}$.

2.2. Extraction of materials from commercial batteries and ageing protocol

As put forward in Section 1, experimental parametrization is carried

out with analyses of cathode material extracted from batteries. In this subsection, we provide details on the battery opening procedure and electrode treatment. This protocol, based on [21], aims to establish a standardized approach minimizing material damaging.

Cathode material is extracted from [16] SONY US18650V3 (Sony V3 18,650Battery, 2250mAh, 10 A, 3.7 V) cylindrical batteries. Samples are obtained from an as formed battery, that has not been subjected to cycling, and an aged one. Of course, the as formed battery has undergone the proprietary commercial electrochemical formation and activation processes, which involve various cycling steps at different C-rates. For simplicity, we shall refer to this "quasi-pristine" condition as "as formed" [30]. The battery is aged according to the 'Cycle life test' outlined in the EN IEC 62660–1 [31] standards (in the following "IEC"), which aims at replicating the effects of degradation caused by the operation of electric vehicle batteries, through a specifically developed stepwise discharge profile (up to 4C maximum rate), also inclusive of regenerative events. For this reason, such "IEC" dynamic discharging cycle test at 45 °C, followed by full C/3 CC-CV charging, is continuously performed in the SOC 100 %–0 % full discharge window for 530EFC (more details are available in [32,33] and in Supporting information (SI)), reaching end-of-life condition. The battery is discharged at minimum cut-off voltage (safe condition) and then opened in an argon-filled glove box to avoid materials side reaction with air and humidity, in particular hydrofluoric acid formation. After cathode extraction, a washing step is applied with electrolyte solvent (DMC (Sigma-Aldrich) to remove residual lithium salt. The electrode is finally dried to remove solvent. One-sided cathodes are needed for electrochemical tests in coin cells and the cathodic material is removed from one of the sides using cotton swabs soaked with N-Methyl-2-pyrrolidone as solvent (NMP). Thus-prepared samples are stored in an argon-filled glovebox until their usage [21].

2.3. Measurement of battery design parameters

(i) Active material elemental composition is quantified with ICP-OES (ThermoScientific iCAP PRO) for a quantitative characterization.

(ii) Macroscopic geometrical parameters (E_W, E_L) are directly measured mechanical gauges and cross-sectional geometrical parameters (E_{TH}, E_{CC}) that evaluated from SEM micrographs. (ii) Microscopic electrode-architecture parameters (ε_{EL}, R_p) are estimated from SEM images, complemented by EDS maps. Quantitative image analysis is performed with customized Phyton script and the outcomes are calibrated against standard Mercury Intrusion Porosimetry (MIP = measurements [34], carried out is a certified external laboratory. SEM images of electrodes are acquired using a field emission-scanning electron microscope (FE-SEM, Zeiss SUPRA 40, Jena, Germany) operating in a high vacuum. In-plane observations are made on the as-extracted material, while cross-sectional ones are based on cathode disks, punched (Ø 12 mm) from the cathode stripes, inserted in a coin cell with the usual spacers and conical spring, to ensure mechanical consistency and then embedded in two-component PolyFast (Struers) black bakelite hot mounting resin with carbon filler., hardened in oven at 176 °C for 5 minuts and sectioned with a Metkon Micracut 202 automatic cutting machine. The cross sections were manually polished with a specifically optimized procedure, consisting of: (i) sequential automatic grinding, employing a Hitech Europe MP3-11 T polishing machine, using SiC abrasive papers of grit numbers: 400, 600, 800, 1200,2500 and (ii) automatic fine lapping, employing a MP 22-22 V machine, with 0.05 μm colloidal alumina suspension and 1 μm diamond paste. The polishing procedure developed, yields high-quality cross-sections without additional surface treatment, such as ion etching. The electrodic material in powder form for SEM particle size measurements are obtained by scraping off the electrode coating and ultrasonicating in Isopropanol (Sigma-Aldrich) (isopropanol/active layer powder proportion of 3 mL/1 mg) at 10 W for 1 min. The resulting well-dipersed suspension of cathodic material is then cast onto glass paper coupons for SEM analysis.

2.4. Measurements of electrode material parameters

The following cathode material parameters D_p, σ_s, $c_{s,max}$ were estimated on the basis of electrochemical measurements. Electrochemical measurements were performed by inserting the cathode material in a coin cell, in different ways as detailed below, and employing a Biologic V300 potentiostat.

(i) D_p was evaluated by GITT. One-sided cathode samples (punched disks Ø 12 mm) were assembled in half-cells with glass fiber separator (WHATMAN GF/A) and Li metal chips (Ø 12 mm, 1 mm thickness). The separator was soaked with 100 μL of electrolyte consisting of 1.0 M LiPF6 in EC/DMC = 50/50 (*v*/v) (Sigma-Aldrich). The cell was subjected to formation treatment consisting of three galvanostatic charge/discharge cycles at C/10 with voltage cutoff values of 3.0 and 4.3, respectively. After formation, GITT measurements were performed in the voltage range 3.6 ÷ 4.2 V alternating charge at C/10 charge for 10 min and OCP relaxation with termination criterion either for 1 h or $dE/dt < 5$ mV h^{-1}). The raw data are post processed with a specifically coded Matlab script. More details on GITT measurements can be found in [35].

(ii) Impedance spectrometry was employed to estimate σ_s. For this purpose, double-sided punched cathode samples 6 mm in diameter are coated with electronically conducting silver paste, contributing 0.1 Ω in the adopted configuration, on both surfaces, in order to achieve an ion-blocking electrode configuration. The Ag paste was dried in atmosphere at ambient temperature and the sample was inserted in a coin cell casing, with the following sequence of components: Spacer | Ag paste | 1st catodic material layer | Al current collector | 2nd cahodic material layer | Ag paste | Spacer | Conical spring. Impedance spectrometry measurements were run without applied bias in the frequency range 0.5 Hz – 5 MHz [36].

(iii) $c_{s,max}$ is estimated with ICP.

2.5. Measurement of Electrokinetic parameters

(i) The OCV parameter can be extracted from the raw data generated in the GITT measurement described above in Subsection 2.4.ii for D_p, with specifically coded Matlab scripts, following the approach detailed in [15,35].

(ii) k and C_{dl} are quantified with Electrochemical Impedance Spectrometry (EIS). EIS measurements were carried out at OCP, applying a with a sinusoidal potential of 10 mV peak-to-peak in the frequency range 10 mHz – 0.5 MHz. In order to estimate E_a with Arrhenius plots, the experiments were performed at the following temperatures: 25–30–40–50–60°°C. In order to carry out EIS measurements in a 3-electrode configuration, we employed a Swagelok cell with extracted cathode as working electrode (Ø 5–6 mm), Li metal chip (Ø 12 mm, 1 mm thickness). as counter electrode and Li (Ø 5 mm, 1 mm thickness).) as the Pseudo Reference Electrode. Prior to EIS measurements, the cell was subjected to a formation treatments consisting in 3 galvanostatic charge/discharge cycles at C/10 with voltage cutoff values of 3.0 and 4.3 V. Fitting of EIS spectra was carried out with a purposely coded Matlab script. Details on EIS modelling and fitting are reported in Section 3.3 and in Supporting information.

3. Results and discussion

3.1. Battery design parameters

3.1.1. Active material composition

Cross-sectional elemental mapping by EDS (Fig. 2A and B) on as formed sample shows a granular structure composed of Co, Mn and Ni oxides. Some of the grains exhibit the joint presence of the three metals, suggesting NMC, while others only contain Mn, hinting at LMO: the cathode material is thus a blend of NMC and LMO: a common solution for automotive applications [37,38]. Quantitative ICP analysis reveals that the actual composition is 83.62 ± 0.2392 % NMC-532, blended with LMO (16.38 ± 0.2392 %), yielding a theoretical capacity of 145 mAh/g [39]. Changes in lithium content due to ageing can be readily detected by ICP, showing a variation from 4.4 % to 4.2 % wt.

3.1.2. Battery geometrical parameters

Electrode and current collector thicknesses E_{TH} and E_{CC} were evaluated from SEM cross-sections (Fig. 2C). E_{TH} was found to be 157.8 μm, the thickness of each active material layer was 60μm and E_{CC} was 18 μm. The overall electrode dimensions E_L e E_W are respectively 565 mm × 57 mm (Fig. 2D). In plane SEM micrographs allowed the qualitative and quantitative mapping of the fractions of void porosity ε_{EL}, along with the active material particle radius R_P. Since the joint volume fractions of conductivity carbon and binder typically amount 5 % or less [39], we identified the solid volume fraction with that of the active material phase. Mapping of porosity and particle size distribution are in principle required because these quantities are controlled by the fabrication process [39], by the calendaring step, in particular [40]. Fig. 2E, F, G and 2.I display a selection of images for both as formed and aged samples, highlighting electrode morphology changes with an evident particle fracture [41]. To quantitatively assess porosity from SEM images, a segmentation algorithm is required to define the appropriate thresholding. We developed a custom code for extracting porosity values from digitized SEM images, building on the approach of [42] and implementing an original, robust thresholding protocol [43,44] (Fig. 2H and J) (More details available in S.I., Fig. S.2 and Fig. S.3) The estimated porosity for as formed and aged samples is 24.7 ± 2.7 % and 27.05 ± 0.79 %, respectively (Table 2). Micrographs captured at representative locations of the as formed cathode are shown in Fig. S.4, confirming a homogeneous porosity distribution and consistent cathode architecture. It is important to note that comparative measurements for the aged cathode are unavailable due to the condition of the electrode following battery disassembly, as a consequence, electrode samples were collected from random positions. To calibrate and validate the imaging-based porosity estimation, we applied MIP. The MIP-derived porosity values for as formed and aged samples are 30.14 ± 1.51 % and 26.51 ± 1.34 %, respectively. Indeed, SEM imaging-based porosity estimates exhibits the limitation of provides 2D information to estimate a 3D property. Nevertheless, this conceptual limitation can be controlled from a theoretical viewpoint [45]. Moreover, on the basis of imaging, it is not possible to discriminate between open and closed pores. MIP, instead, offers direct 3D information and is exclusively responsive to open porosity. Still, the 3D information remains more important rather than 2D one. For this reason, the optimal approach would likely involve using MIP on a limited number of small samples (time saving from the experimental point of view) to establish a reliable reference scale. These results could then be utilized to calibrate the filters applied to 2D SEM images, enabling the non-destructive analysis of a larger number of samples. This combined methodology ensures both the robustness and scalability of the porosity analysis. Despite the differences in the methodologies, the measured values are in close agreement within the standard error (considering the typical 2–3 % experimental uncertainties in cathode porosity measurements [34]). From our experimental results, it can thus be concluded that cathode porosity is essentially the same in the two conditions investigated [46].

The active material particle radius R_p was evaluated again from SEM images of the powder scaped off from the active layer (Fig. 2K and M). Over 1000 particles were analysed using the Cvat™ [47] segmentation tool to identify spheroidal particles and to determine their radius, R_p. An example of the segmentation for both as formed and aged active particle populations is presented in Fig. 2L and N, with additional examples available in the supporting information (Fig. S.5). The as formed catholic material particles exhibit well defined spheroidal shape and residual conductivity carbon and binder do not affect the estimation of R_p, thatagain averaging on all investigated positions results to be R_P 7.19 ± 1.39 μm (Table 2). The radius of aged particles exhibits significant variability, with an average R_p of 5.91 ± 2.25μm (Table 2), along with the presence of smaller particles. A detailed analysis and fitting of the particle size distribution histogram reveals a Gaussian distribution for as formed particles (Fig. 2O and P) whereas a Weibull distribution better fits the aged particles (Fig. 2Q and R), indicative of particle fragmentation [48,49].

On the basis of the quantities previously estimated in this Section, it is possible to evaluate the other two electrode geometrical parameters that are required for P2D model: (i) The electrochemically active surface area (ECSA), quantifying the interface between the porous electrode and the electrolyte and (ii) the electrode surface area per unit volume a, measuring the amount of surface area available for electrochemical reactions, relative to the volume of the electrode material [50].

These quantities are defined as follows: $ECSA = \frac{\varepsilon_{AM} V_{el}}{V_p} S_p$ and $a_k = \frac{3\varepsilon_{AM}}{R_p}$ where: V_p is the particle volume; S_p is the particle surface area (that can be estimated by assuming monodisperse spherical particles); V_{el} is the electrode geometry volume that can be computed by multiplying together electrode geometrical area and E_{TH}. For the studied electrode ECSA and a_k are respectively equal to 30.91 ± 21.56 cm^2 and 291.6 ± 19.45 mm^{-1} for as formed, and 39.38 ± 54.15 15 and 371.46 ± 47.26 mm^{-1} (15 Ø mm electrode).

3.2. Electrode material parameters

3.2.1. Li^+ diffusion coefficient

Diffusion coefficient D_p as a function of SOC is estimated from GITT data [35,51].GITT electrochemical signal is shown in Fig. 3.A along with the salient features of a GITT measurement (Fig. 3.B), by employing a sequence of galvanostatic pulses followed by relaxation periods, it is possible to derive the diffusion coefficient (D_p) [35–37]. More detailed explanations of the GITT methodology and its operation are provided in S.I. The as formed and aged samples exhibit distinctly different responses to the GITT test (Fig. 3A and C): the estimated diffusion coefficient values as a function of intercalation degree is reported in Fig. 3D. Despite the considerable variability encountered in the literature and the inherent complexity of the diffusion mechanism in a blended cathode, the values appear to be within an acceptable range [52]. For the aged sample, fewer GITT steps are required to cover the voltage window. Generally, the diffusion coefficient of the aged sample is higher than that of the as formed one, although the diffusivity of the as formed sample increases with the degree of delithiation, as expected, while the aged sample shows a less consistent trend. It is also noteworthy that the voltage signal values differ significantly between the two samples. The as formed sample exhibits a more uniform profile, whereas the aged sample presents a wider variety of slopes (Fig. 3C). According to the literature [53], various factors can influence the GITT-derived values, with the most significant likely being the altered particle size of the aged electrode, which directly affects the numerical value of the diffusion coefficient (as derived from the approximate formula employed for the standard data analysis) and indirectly the steady-state and total voltage changes. Other explanations for the response of this analysis could be the alteration of the active material, with NMC or LMO working in suboptimal way [54]. One hypothesis stems from existing literature [54], which discusses the interaction between NCM and LMO,

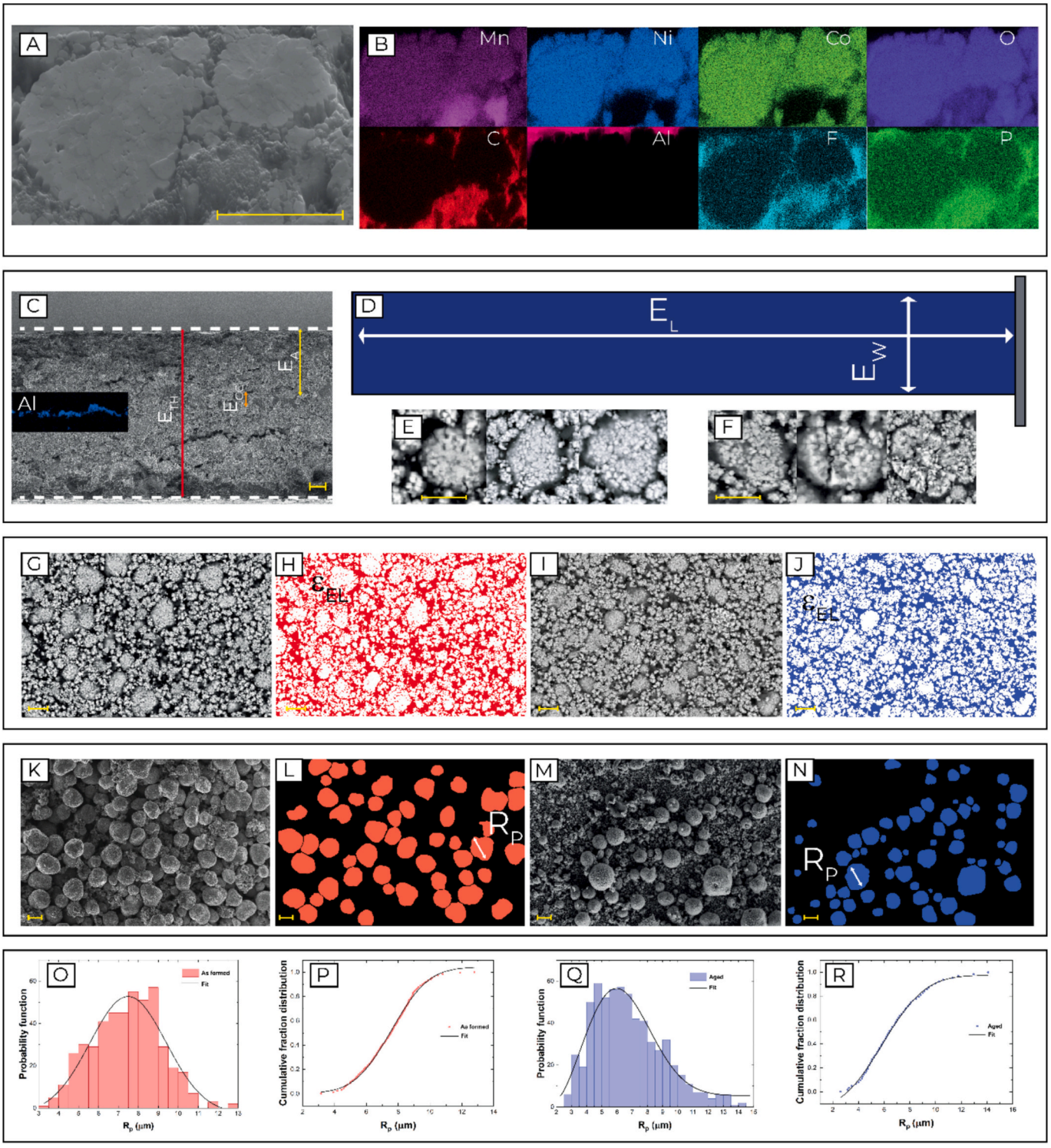

Fig. 2. Battery design parameters. (A) Cross-sectional SEM micrographs of the cathode active layer and (B) corresponding EDS elemental maps. (C) Typical SEM cross-section of the cathode with two-sided active material coating. Total electrode thickness (red arrow), active material thickness (yellow arrow) and current collector thickness (orange arrow). The inset with the EDS Al map highlights the position of the current collector. (D) Unrolled electrode total dimensions; SEM details of as formed (E) and aged (F) active particle. Selection of in-plane SEM images for as formed (G, H) and aged (I, J) samples, along with the respective image segmentations for porosity evaluation. Typical SEM images of powder extracted from the active layer of the cathode for image segmentation: as formed (*K*,*L*) and aged (M, N), along with their respective segmented images. Analysis of particle size distribution for as formed (O) and aged (Q) extracted powder, including (P) linear fitting of the cumulative function distribution for as formed powder and (R) Weibull fitting with the cumulative fraction distribution for aged one. Yellow scale bar: 10 μm. (For interpretation of the references to colour in this figure legend, the reader is referred to the web version of this article.)

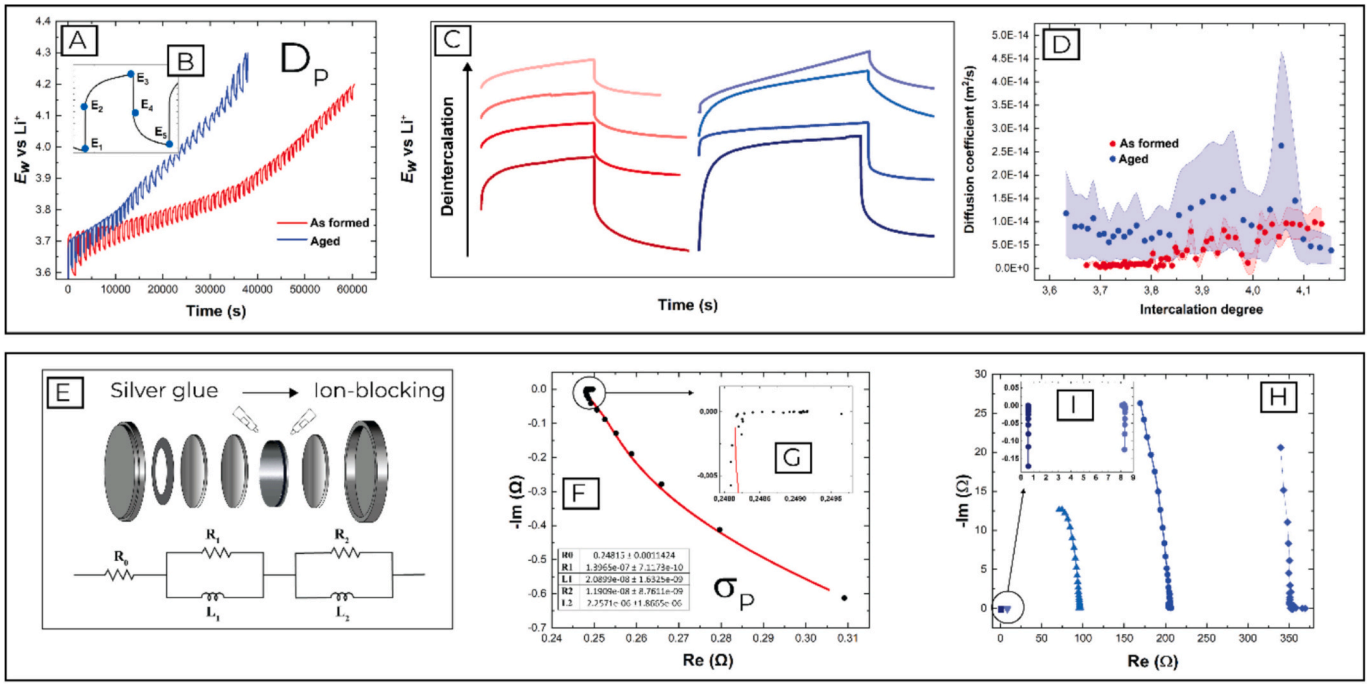

Fig. 3. Electrode material parameters. (A) Schematic of a GITT measurement; showing the imposed galvanostatic sequence and (B) the corresponding potential response for as formed and aged electrode. (C) Potential time transient trend evolution with intercalation degree. (D) Diffusion coefficient as a function of intercalation degree with the corresponding confidence intervals. (E) Equivalent electronic circuit model employed for data fitting and coin cell assembly for the electronic conductivity measurements. (F) Typical Nyquist plot and fitting for as formed electrode, along with fitting parameters with (G) inset showing the high frequency region. (H) Solid electronic conductivity variability for aged cathode: inset (I) highlights the low-resistance results.

particularly their mutual exchange of lithium ions. It is plausible that the NCM in our samples has undergone significant degradation, thereby limiting its ability to support LMO activity. NCM operates in the voltage range of 3.6–4.0 V, at which point LMO becomes active. GITT measurements reveal marked differences in the voltage range associated with NCM: aged materials reach the working potential of LMO earlier, while the voltage window between 4.0 and 4.3 V (specific to LMO) shows similar transient times for both fresh and aged electrodes. The pronounced differences in transient behaviour in the LMO region could suggest that degraded NCM attempts to compensate for LMO inefficiencies. Additionally, the possibility that LMO itself plays a more active role in some inefficiencies cannot be excluded.

Nevertheless, confirming this hypothesis would require advanced material characterization under in situ or in operando conditions, which are beyond the scope of this study. As our experimental protocol (EBP) is designed to be an accessible and straightforward laboratory method, such advanced techniques were not employed.

In the absence of additional measurements, the most evident and robust explanation lies in the particle size dependency. As discussed in the manuscript, the diffusion coefficient is derived from Fick's law and relies on the R_p parameter. An increased confidence interval for R_p, indicative of greater variability, directly impacts the calculated diffusion coefficient. The significant variance in R_p observed for aged electrodes undoubtedly contributes to the observed diffusion coefficient variability. Consequently, we have highlighted particle size effects as the primary explanation while acknowledging the potential influence of suboptimal interactions between the two materials. A more in-depth analysis of this aspect is beyond the scope of the present work as well as inconsistent with the conceptual scope of the GITT method, that is admittedly an integral one, based on strong hypotheses, nevertheless yielding rough, but practically useful and comparatively significant indicative estimates.

Finally, also the Open Circuit Voltage (OCV) as a function of intercalation degree was derived from GITT data [29], as commented in Section 3.2.2 and represented in Fig. 4O, demonstrating the increased irreversible polarizability of the aged cathode.

3.2.2. *Electronic conductivity*

The P2D model requires knowledge of the effective electronic conductivity of the cathodic active layer $\sigma_{s,eff}$. This can be evaluated combining the electronic conductivity of the solid phase σ_s (comprising cathodic active material and conductivity carbon) and the electrode tortuosity ε in a Brugmann-type correlation [5]. In our context, EIS directly unveil $\sigma_{s,eff}$ as the measurements is conducted at the electrode-level rather than on the single active material.

Impedance spectrometry measurements carried out with the cell described in Section 2.4. (Fig. 3E) show purely resistive behaviour (Fig. 3F and G), confirming ion-blocking behaviour. It is worth noting that the presence of the aluminium current collector does not influence the result, since its electronic conductivity it is more than one order magnitude larger than that of conductivity carbon [35]. Significant differences emerge when comparing the as formed and aged samples. The cathodic material from the as formed sample exhibits a low electronic conductivity variance (31.4 ± 0.01 S m^{-1}, Table 2). In contrast, the aged sample shows substantial variability ranging from 8.43 ± 0.01 to 0.012 ± 0.001 S m^{-1} (Table 2) indicating that large regions of the electrode exhibit reduced electronic conductivity. This results in a final electrode behaviour resembling a current divider, with distinct zones of high and low conductivity (Fig. 3I and H). For our purpose, we selected only the region capable of sustaining electron flow to represent the entire electrode and to derive the input parameters for the P2D model. Once again, the considerable variability observed underscores the limitations of the P2D structure in accurately modelling the aged battery.

3.2.3. *Maximum Li$^+$ concentration*

This quantity was obtained from ICP measurements, yielding values of 30,687 ± 1641 mol m^{-3} for the as formed sample and 27,970 ± 744 mol m^{-3} for the aged one (Table 2), indicating a slight reduction in

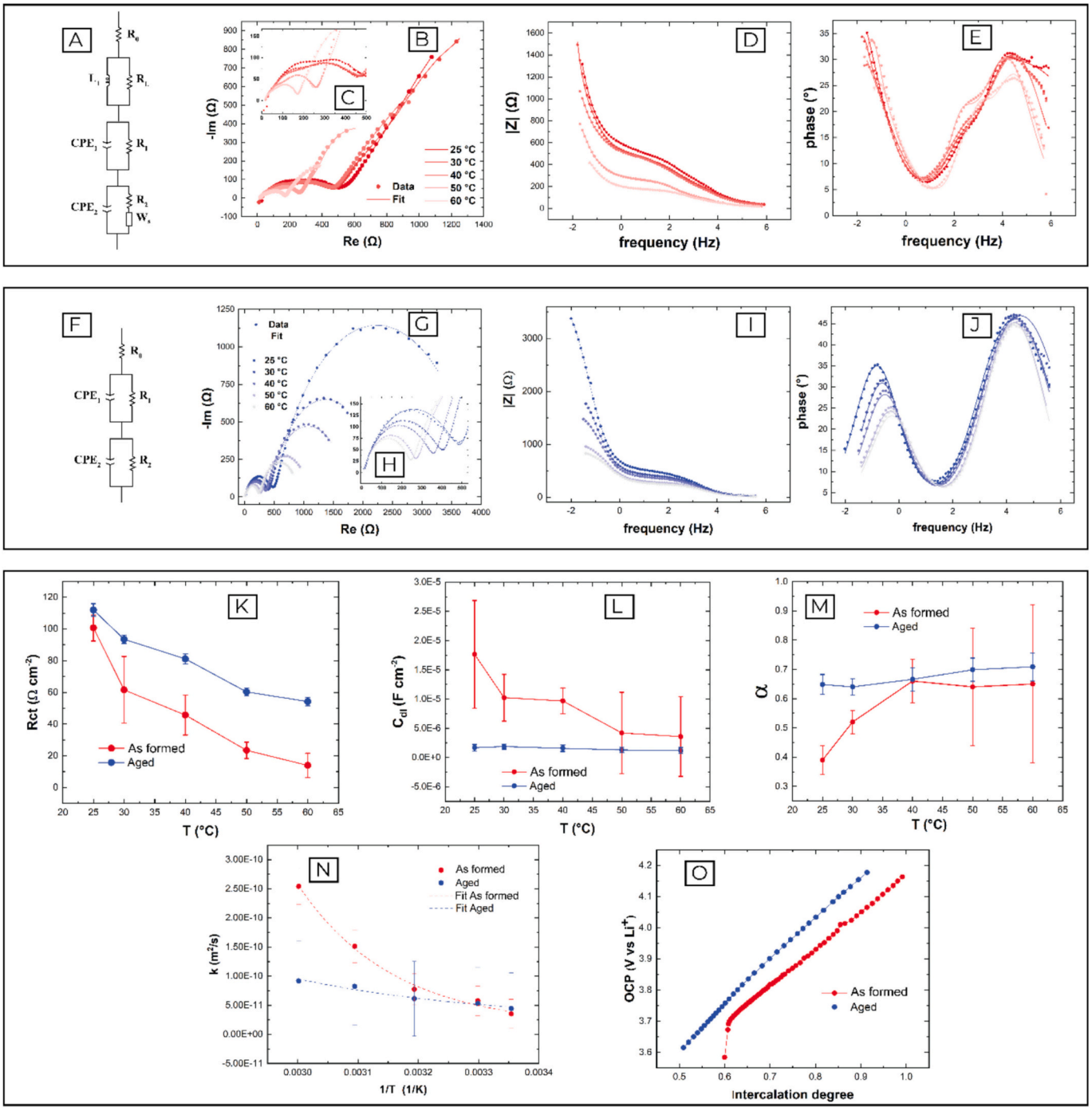

Fig. 4. Electrochemical thermodynamic and kinetic parameters. (A, F) Equivalent electronic circuit models for as formed and aged samples with temperature-dependent Nyquist (B, C, G, H) and Bode (D, E, I, J) plots. (K-M) Temperature-dependent EIS parameters: (K) R_{ct}, (L) C_{dl} (scaled with ECSA) and (M) α. (N) Temperature-dependent reaction rate k with Arrhenius exponential fit. (O) OCV as a function of intercalation degree: the potential window corresponds to that of practical battery operation.

lithium inventory available for electrochemical reduction [41]. It is worth highlighting that it is customary in the literature to estimates the maximum lithium concentration by assuming the material is fully lithiated at its stoichiometric limit [15]. While this approach is sound for pristine materials, its reliability can be questionable for both as formed and aged samples due to SEI formation and electrode degradation, affecting the stoichiometry. In any case, some degree of loss of lithium inventory is expected on the basis of the battery discharge protocol applied prior to opening, whereby: (i) the battery voltage was brought to minimum cut-off voltage (fully discharged state) before opening; (ii) the half-cell galvanostatic capacity estimation (C-rate C/10) required only 10 min to reach the discharge cutoff at 2.5 V, starting from an initial voltage of 3.6 V. These circumstances are strongly indicative of the fact that the cathodic material was fully intercalated. Considering the stoichiometric lithium concentration in the LMO-NMC532 blend, along with the experimentally determined electrode coating mass and the electrode's volumetric dimensions, $C_{s,max}$ was calculated to be 49,796 ± 975 mol m^{-3}, showing a 40% deviation from the ICP measurements. This discrepancy highlights the necessity of using ICP or other quantitative methods to verify or refine estimates of maximum lithium

concentration, rather than relying solely on theoretical assumptions.

3.3. Electrochemical thermodynamic and kinetic parameters

The electrokinetic parameters: reaction rate k, activation energy E_a and double layer capacitance C_{dl} have been extracted from EIS measurements. Parameter estimates have been carried out in fully-intercalated conditions with material as extracted from a battery after formation cycle (see Section 2.5) for both as formed and aged sample, and scaled them for the respective ECS. Temperature-dependent EIS spectra, in Bode and Nyquist forms with their fits and the equivalent-circuit model used to fit the experimental data are reported in from Fig. 4A to 4J. It worth mentioning that the fitting process required different equivalent electrical circuits, again highlighting a clear effect of ageing. The EIS spectra measured in this work are compatible with literature results for as formed blended NMC and LMO [38], but exhibit characteristic differences due to the interaction of the two active materials. In fact, the electrochemical behaviour of the blended NMC-LMO electrodes is controlled by either oxide, depending on the battery SOC: at low (almost completely intercalated cathode) and high (almost completely deintercalated cathode) SOCs NMC and LMO prevail, respectively [38]. Fig. 4.A sketch the as formed electrical circuit model. The high-frequency RC semicircle is essentially associated with the contact resistance between the active layer and the current collector, while the lower frequency RC semicircle is controlled by charge transfer at the solid-electrolyte interface [55]. The individual contributions of NMC and LMO lead to overlapping RC semicircles, that cannot be straightforwardly distinguished by impedance analysis [56]. The electrical circuit model incorporates: resistances, capacitances, and Fractal Warburg impedances [57–60] to represent the electrolyte resistance, charge transfer, and mass transport contributions, respectively. Additionally, the model takes into account non-idealises such as anisotropic diffusion and variations in particle sizes. More details on the electrical circuit component, the fitting model description and an on the applied methodology are available in S.I.

A dedicated equivalent electrical circuit model (Fig. 4F) is required to track degradation, as the EIS spectra differ significantly. To the best of the authors' knowledge, no electrical circuit model is currently available in the literature for representing the blended aged cathode. Some models, instead, exist for aged pure NCM [61] and LMO [62] cathodes. The Nyquist plot features suggest that the contact and charge transfer resistances either merge into a single semicircle or that new spectral features appear, whence the two cannot by numerically discriminated since their frequencies are very close, Fig. 4D, E, I, J. In the literature, similar scenarios have been attributed either to degradation processes [63] or to the dominance of one active material over the other one [64]. It is important to note that the objective of this study is to parameterize both as formed and aged batteries for P2D modelling, where the parameters should capture the electrode behaviour rather than the precise material properties. For this reason, the capacitance and charge transfer resistance associated with the higher frequency arc are selected for parameter estimation. High quality fitting the EIS spectra is possible with this model, obtaining physically meaningful parameters with reasonable confidence intervals and excellent parameter continuation as a function of temperature (see Fig. 4 and Table 1).

The temperature dependence of R_{ct} and C_{dl} are shown, respectively, in Fig. 4K, L and M. As expected, R_{ct} decreases with temperature owing to Arrhenius kinetics and C_{dl} decreases owing to molecular agitation lowering the dielectric permittivity of the electrolyte [65,66]. R_{ct} was found to increase in the case of the aged electrode, while C_{dl} decreases. This behaviour can be attributed to particle fracture, changes in porosity, and the formation or thinning of the cathode-electrolyte interphase (CEI) [63].

The rate constant k is not directly included among the EIS parameters, but it can be obtained from them through equation: $k = \frac{2RT}{R_{ct}SFC_s^{max}\sqrt{C_e}} \times \frac{\sqrt{C_{e,ref}}}{F}$, where T is the absolute temperature, R is the gas constant, S is the electrode electrolyte surface area (4.95 cm^2 for as formed and 4.37 cm^2), F is the Faraday constant, C_s^{max} is the maximum Li concentration and C_e is the Li^+ concentration in the electrolyte and $C_{e,ref}$ is 1 $kmol/m^3$ [20]. Fig. 4N sketches the k exponential trend of *k* with T with the corresponding Arrhenius fits to estimate the activation energy E_a, that result to be 44.71 ± 3.3 and 17.19 ± 1.44 kJ/mol for as formed and aged NCM-LMO, respectively. It is worth noting that the confidence intervals are larger for the aged sample, mainly owing to the modified R_p distribution. Our results show that *k* values for as formed and aged cathodes are similar at ambient temperature, while their behaviour diverges at higher temperatures. Our accurately estimated E_a (Table 2) values seem to contrast the common-sense expectation that the as formed cathode would exhibit faster charge-transfer kinetics, owing to an allegedly more ordered crystalline structure and lower defect density. In fact, it results the material evolution brings about an improvement of both charge-transfer, alongside with that of mass-transport rate, as shown in Section 3.2.1, that are however accompanied by a deterioration of the electron transport rate, resulting in overall degradation of electrokinetics.

Despite this, the lower E_a values found for the degraded cathode is clearly fenomenologically documented in the literature [67–71], even though limited attention has been devoted to its physical origin [67]. Nevertheless, this seemingly paradoxical result is fully compatible with the still very limited state-of-the-art fundamental understanding of the activation barrier scenarios for charge transfer processes at intercalation electrodes. In fact, this is a very complex problem, because the full complexity of the host/electrolyte interface composition and structure - including desolvation, adsorption and interfacial charge-separation processes – should be taken into account to build a definitive picture of the underlying energy scenario [72]. Moreover, as recently pointed out, the CEI structure, the CEI/active material interface [73] as well as

Table 2
Summary of Estimated Parameters for as formed and aged samples.

	As formed	Aged
Electrolyte volume fraction % (ε_{el})	30.1 ± 1.5 %	26.5 ± 1.3 %
Mean particle radius (R_k) [um]	7.18 ± 1.39	5.91 ± 2.25
Solid phase Diffusion coefficient (D_s)(mean) [m^2/s]	Fig. 3 D	
Solid phase electronic conductivity (σ_s) [S m^{-1}]	31.45 ± 0.01	8.43 ± 0.01
Maximum concentration ($C_{s,k}$) [kmol/m^3]	30.7 ± 1.6	28.0 ± 0.7
Open Circuit Voltage (OCV) [V]	Fig. 4 P	
Reaction Rate k [m^2/s]	see Table 1	
Double layer capacitance (C_{dl}/cm^2)	see Table 1	
Activation energy [kJ/mol]	44.71 ± 3.31	17.19 ± 1.44

Table 1
Fit parameters for the EIS spectra and model of Fig. 4 for as formed (P) and aged (A) sample, parameters are scaled with ECSA.

	25 °C		30 °C		40 °C		50 °C		60 °C	
	P	A	P	A	P	A	P	A	P	A
R_{ct} [Ω/cm^2]	100.7	111.9	61.6	93.5	45.7	81.1	23.5	60.3	13.9	54.1
j_0 [A/cm^2]	1.04E-5	1.33E-6	1.71E-5	1.59E-6	2.30E-5	1.84E-6	4.48E-5	2.47E-6	7.53E-5	2.75E-6
k [m^2 /s]	3.52E-11	4.44E-11	5.75E-11	5.32E-11	7.76E-11	6.13E-11	1.51E-10	8.24E-11	2.53E-10	9.18E-11
C_{dl} [F/cm^2]	1.76E-5	1.67E-6	1.02E-5	1.88E-6	9.68E-6	1.57E-6	4.21E-6	1.28E-6	3.58E-6	1.19E-6

the dynamic details of the active material structure [74] play a role that can become overwhelming in the control of the actual activation energy value.

Thus, at the moment, activation energy prediction is possible only with model materials and systems, interpreted with quantum-mechanical approaches. Therefore, experimental results with realistic materials are not liable of a straightforward, unambiguous physical interpretation. One possible explanation found in the literature is the loss of active lithium, which reduces the energy barrier for the reaction [67,68]. Specifically, the reduction of the Li $c_{s,max}$ found in our work is coherent with our E_a estimates.

3.4. Discussion of parameter estimates and EBP relevance

3.4.1. Comparison with other literature parametrization tools estimation

The importance of experimental parameterization has been pinpointed in a close-knit group of publications. In fact, positive measurements with appropriate physico-chemical techniques can provide a precise evaluations of the actual numerical values of relevant material properties. Of course, the downside of this approach is that it is expensive, time-consuming, destructive, and – before specialized *in operando* methods are developed – limited to post mortem applications [75].

Work in the field includes Ecker et al. [14], Schmalstieg et al. [20], Oca et al. [76], and Chen et al. [15]. These studies parameterize experimentally all battery components with model validation. However, these works focused exclusively on pristine batteries. Our present work, in addition to proposing novel approaches to parameter estimate is also used to assess the changes of parameter values upon battery ageing.

In our study, we've also aimed to refine steps of these methodologies, making them simpler and more widely accessible for laboratory use. These studies share the goal of parameterizing lithium-ion batteries with respect to mathematical modelling, but they differ in their methodologies. While Ecker et al. [14] and Schmalstieg et al. [20] apply MIP for porosity estimation, Oca et al. [76] and Chen et al. [15] combine FIB-SEM with MIP/BET. As mentioned in Section 3.1.2 and in the Supplementary Information (S.I.), MIP is an excellent tool for porosity estimation, but it lacks detailed knowledge about closed pores. FIB-SEM, on the other hand, requires specialized skills and equipment that are not widely available, and it faces challenges in 3D image reconstruction [77] and segmentation. In our work, we propose to combine SEM and MIP, and we provide a critical discussion of the proposed approach.

Moreover, while [14,15,20,76] all use 4-probe electrical characterization methods, we propose an alternative approach that establishes electrode-level conductivity parameters without relying on the Brugman correlation with material electronic conductivity (details provided in Subsection 3.2.3).

Like the other studies, we also implement GITT and EIS to measure diffusion coefficients and electrokinetic parameters. However, we also estimated Cdl, that is required for transient simulations, including the modelling of EIS spectra.

3.4.2. Comparison with literature work on NCM-LMO cathodes

Moreover, it is worth nothing that the systematic parametrization studies [14,15,20,76] do not consider blended cathodes with multiple active material. Instead [12,78–80] report partial experimental parametrization of NCM-LMO blended composition.

In particular, [80] report particle radius estimates in the range 4.5–7.5 μm, differentiating between LMO and NCM particles with SEM-EDS imaging. This range closely matches our values, especially considering their unspecified blended composition, which could affect the R_p based on the NCM/LMO ratio (larger NCM particles contribute higher values). They also report a porosity ε_{EL} of 0.25, consistent with our findings. However, their electronic conductivity σs is 6.2 $S{\cdot}m^{-1}$, showing some discrepancy with our results, though further discussion is limited as they do not detail their analytical methods. Other geometrical parameters such as E_{TH}, E_{CC}, E_L, E_W, depend heavily on cell type and manufacturer, making direct comparisons irrelevant.

Remaining parameters like D_p are partially consistent with our findings, with Jung reporting values ranging from $5.5{\cdot}10^{-14}$ (NCM) to $2.5{\cdot}10^{-13}$ (LMO). This variability aligns with our discussion in Section 3.2.1. However, electrokinetic parameters are not reported in Mao et al. [78] and are likely measured, without specifying references and methods.

Mao et al. [78] focus on estimating the composition of blended electrodes from experimental voltage curves. In addition, they consider the dimensions of the primary particles R_p, which is an order of magnitude lower than our secondary particle values. Their estimates of the diffusion coefficient D_p range from $1.44{\cdot}10^{-13}$ (NCM) to $6.6{\cdot}\ 10^{-15}$ (LMO), different from those reported in [78], where D_p is found to be higher for NCM than for LMO. $C_{s,max}$ estimates vary between 23.339 (LMO) and 49.761 (NCM) $kmol/m^3$, correlating with theoretical capacity. Table S.1 provides an overview of the total estimated parameters in these publications.

These numerical discrepancies in very similar materials, emphasize on the one hand the importance of experimental parametrization tool, such as EBP and, on the other hand, the necessity of a clear and critical discussion of the measured parameters.

3.4.3. Parameters evolution with ageing and possible impact on the P2D model

In this Section, we comment jointly the outcomes of the individual parameter estimates for as formed and aged electrodes.

Structural parameters evolve as ε_{EL} increases from 24.7 % to 27.05 %, attributed to particle fractures observed via scanning electron microscopy. Concurrently, the average particle radius decreases from 7.19 μm to 5.91 μm, with size distributions shifting from Gaussian to Weibull. This fragmentation enlarges the electrochemically active surface area from 30.91 cm^2 to 39.38 cm^2 and raises the specific electrode area per volume from 291.6 mm^{-1} to 371.46 mm^{-1}, enhancing reaction sites despite ongoing structural deterioration.

Material properties also transform significantly. The lithium diffusion coefficient becomes generally higher and less consistent in aged materials due to fragmentation and particle properties. $C_{s,max}$ decreases from 30.7 mol/m^3 to 28 mol/m^3, indicative of diminished lithium availability. $\sigma_{s,eff}$ regions form, creating a heterogeneous electrical distribution of electronic conductivity in the electrode.

Electrokinetic changes include increased R_{ct} to owing to particle fractures and cathode electrolyte interphase (CEI) interactions, while double-layer capacitance C_{dl} decreases due to electrode structural modifications, such as porosity variation. Despite a stable charge transfer rate constant k between as-formed and aged samples, the activation energy for charge transfer drops significantly from 44.71 kJ/mol to 17.19 kJ/mol, probably caused by loss of lithium inventory. However, these gains are overshadowed by ageing-induced polarization losses, reflecting greater electrochemical inefficiencies.

These findings provide guidelines for model improvement.

One critical consideration is the evolution of R_p, which suggests the necessity of implementing a statistical distribution of particle sizes within the model. The classic monodimensional particle system, while partially effective for pristine batteries (given their inherent size distribution), falls short in describing the complexities of aged systems. Since R_p influences the derivation of multiple parameters, a more nuanced representation of particle size variability is essential to accurately model aged batteries.

Similarly, the observed decline in solid-state electronic conductivity points to heterogeneous electrical conductivity within the electrode. Incorporating this phenomenon into the model may require rethinking how σ_s is represented—moving beyond a simple averaged value to reflect localized disconnections. For example, the model could account for localized disconnections by either reducing the amount of active particles in the P2D model or introducing an idealized additional loss factor to represent electrical disconnections.

Based on the comprehensive analysis of parameter evolution in as-formed and aged electrodes, it is evident that battery degradation introduces multifaceted changes that challenge conventional modelling approaches. By addressing the limitations of the monodimensional particle representation and introducing mechanisms to account for localized electrical disconnections, future models could achieve greater predictive accuracy.

4. Conclusions

This research focuses on the challenges associated with parameter estimation accuracy in battery mathematical modelling, prototypically, but not exclusively, referring to the Newman pseudo-two-dimensional (P2D) model. The traditional approach of relying on literature sources for parameter values results in a strong limitation of the scope of the models and misses important guidelines for model development, in view of parametrising more realistically and flexibly the properties of real present- and next-generation- LIB chemistries. The approach proposed in this work is to develop a protocol for Experimental Battery Parameterization (EBP) to generate model parameters. The comparison with previous works highlights both the strengths and limitations of existing models and parameterizations, underlining the necessity of a more tailored approach. The discrepancies in certain parameters, such as electronic conductivity and diffusion coefficients, emphasize the importance of developing a robust and customized EBP method. EBP not only ensures more accurate model predictions but also provides flexibility to adapt to different battery chemistries, facilitating a more precise understanding of electrode performance.

The proposed EBP includes standard analytical and simple electroanalytical methods: inductively coupled plasma-mass spectrometry (ICP-MS); scanning electron microscopy (SEM) with energy-dispersive X-ray spectroscopy (EDS); galvanostatic polarization (GS); electrochemical impedance spectrometry (EIS), and galvanostatic intermittent titration technique (GITT). In this first work we analysed the cathode material (NMC523-LMO) extracted from otherwise identical as formed and aged discharged commercial batteries.

Specifically, we estimated numerical values of the following model parameters: electrode width (E_W) and length (E_L); current collector thickness (E_{CC}); electrode porosity (ε_{EL}) - evaluated with complementary methods, based on imaging and physico-chemical analyses -; active material particles radius (R_p); solid phase lithium diffusion coefficient (D_p); open circuit voltage (OCV), reaction rate (k); double layer capacitance (C_{dl}); activation energy (E_a), equilibrium Li^+ concentration ($c_{s,max}$) and exchange current density (j_0).

Ageing effects play a pivotal role in altering the structural and electrochemical properties of the electrodes.

Results show, a narrow increase in porosity, accompanied by a decrease in the average particle radius and a shift in particle size distribution from Gaussian to Weibull. These structural changes led to an increase in the electrochemically active surface area and a higher specific electrode area per volume, enhancing reaction sites despite the ongoing structural degradation. Moreover, the lithium diffusion coefficient, exhibited greater variability in aged materials, suggesting that particle fragmentation and lithium loss impact lithium availability. Additionally, the analysis of electronic conductivity revealed the emergence of regions with heterogeneous conductivity, while the charge transfers resistance (R_{ct}) increased due to particle fractures and interactions with the cathode electrolyte interphase (CEI).

Finally, our findings call for the integration of more sophisticated representations of particle size distribution and localized conductivity variations, which are crucial for accurately modelling the behaviour of aged batteries.

Acknowledgment and funding sources*

- The Authors gratefully acknowledge Roberto Losi's (Department of Energy, Politecnico di Milano) contribution to the mercury intrusion porosimetry measurements.

- Co-funding was received from ZnOrgBat project (no. 23034) under the EIT Raw Materials, part of the Horizon Europe funding scheme.

- This study was carried out within the MOST – Sustainable Mobility Center activities funded from the European Union Next-GenerationEU (PIANO NAZIONALE DI RIPRESA E RESILIENZA (PNRR) – MISSIONE 4 COMPONENTE 2, INVESTIMENTO 1.4 – D.D. 1033 17/06/2022, CN00000023). This manuscript reflects only the authors' views and opinions, neither the European Union nor the European Commission can be considered responsible for them.

CRediT authorship contribution statement

Francesco Tavola: Writing – review & editing, Writing – original draft, Visualization, Validation, Supervision, Software, Methodology, Investigation, Formal analysis, Data curation, Conceptualization. **Andrea Casalegno:** Writing – review & editing, Visualization, Formal analysis, Conceptualization. **Gabriele Sordi:** Visualization, Validation, Formal analysis, Data curation. **Claudio Rabissi:** Writing – review & editing, Writing – original draft, Visualization, Investigation, Conceptualization. **Benedetto Bozzini:** Writing – review & editing, Writing – original draft, Visualization, Validation, Supervision, Resources, Project administration, Funding acquisition, Formal analysis, Data curation, Conceptualization.

Declaration of competing interest

The authors declare that they have no known competing financial interests or personal relationships that could have appeared to influence the work reported in this paper.

Appendix A. Supplementary data

Supplementary data to this article can be found online at https://doi.org/10.1016/j.est.2025.116180.

Data availability

Data will be made available on request.

References

[1] J. Le Houx, D. Kramer, Energy Rep. 6 (2020) 1–9.
[2] F. Brosa Planella, W. Ai, A.M. Boyce, A. Ghosh, I. Korotkin, S. Sahu, V. Sulzer, R. Timms, T.G. Tranter, M. Zyskin, S.J. Cooper, J.S. Edge, J.M. Foster, M. Marinescu, B. Wu, G. Richardson, Prog. Energy 4 (2022) 042003.
[3] S.S. Madani, C. Ziebert, M. Marzband, Symmetry (Basel) 15 (2023) 1597.
[4] J.M. Reniers, G. Mulder, D.A. Howey, J. Electrochem. Soc. 166 (2019) A3189–A3200.
[5] M. Doyle, T.F. Fuller, J. Newman, J. Electrochem. Soc. 140 (1993) 1526–1533.
[6] T.F. Fuller, M. Doyle, J. Newman, J. Electrochem. Soc. 141 (1994) 1–10.
[7] M. Doyle, J. Newman, A.S. Gozdz, C.N. Schmutz, J. Tarascon, J. Electrochem. Soc. 143 (1996) 1890–1903.
[8] G. Plett, Battery Management Systems, Volume I: Battery Modeling, Artech, 2015.
[9] J. Newman, K.E. Thomas-Alyea, Electrochemical Systems, Wiley, 2004.
[10] M. Frittelli, I. Sgura, B. Bozzini, Math. Eng. 6 (2024) 363–393.
[11] J.-S. Kim, D.-C. Lee, J.-J. Lee, C.-W. Kim, Sci. Rep. 10 (2020) 15586.
[12] C. Rabissi, G. Sordi, A. Innocenti, A. Casalegno, J. Energy Storage 59 (2023) 106435.
[13] L. Yin, A. Björneklett, E. Söderlund, D. Brandell, J. Energy Storage 39 (2021) 102648.
[14] M. Ecker, S. Käbitz, I. Laresgoiti, D.U. Sauer, J. Electrochem. Soc. 162 (2015) A1849–A1857.
[15] C.-H. Chen, F. Brosa Planella, K. O'Regan, D. Gastol, W.D. Widanage, E. Kendrick, J. Electrochem. Soc. 167 (2020) 080534.
[16] M. Andersson, M. Streb, J.Y. Ko, V. Löfqvist Klass, M. Klett, H. Ekström, M. Johansson, G. Lindbergh, J. Power Sources 521 (2022) 230859.
[17] A.S.L. Ivonne Sgura, B. Bozzini, Inverse Probl. Sci. Eng. 27 (2019) 618–647.
[18] I. Sgura, B. Bozzini, Int. J. Non Linear Mech. 40 (2005) 557–570.
[19] I. Sgura, L. Mainetti, F. Negro, M.G. Quarta, B. Bozzini, J. Comput. Sci. 66 (2023) 101900.

[20] J. Schmalstieg, C. Rahe, M. Ecker, D.U. Sauer, J. Electrochem. Soc. 165 (2018) A3799–A3810.
[21] T. Waldmann, A. Iturrondobeitia, M. Kasper, N. Ghanbari, F. Aguesse, E. Bekaert, L. Daniel, S. Genies, I.J. Gordon, M.W. Löble, E. De Vito, M. Wohlfahrt-Mehrens, J. Electrochem. Soc. 163 (2016) A2149–A2164.
[22] R.F. Ziesche, N. Kardjilov, W. Kockelmann, D.J.L. Brett, P.R. Shearing, Joule 6 (2022) 35–52.
[23] M. Ebner, F. Geldmacher, F. Marone, M. Stampanoni, V. Wood, Adv. Energy Mater. 3 (2013) 845–850.
[24] L. Almar, J. Joos, A. Weber, E. Ivers-Tiffée, J. Power Sources 427 (2019) 1–14.
[25] J. Nájera, J.R. Arribas, R.M. de Castro, C.S. Núñez, J. Energy Storage 72 (2023) 108016.
[26] E. Marchegiani, F. Ferracuti, A. Monteriù, L. Jin, M. Rossi, G. Comodi, L. Ciabattoni, J. Energy Storage 72 (2023) 108591.
[27] A. Lamorgese, R. Mauri, B. Tellini, J. Energy Storage 20 (2018) 289–297.
[28] J. Kim, H. Chun, M. Kim, S. Han, J.W. Lee, T.K. Lee, J. Energy Storage 42 (2021) 103077.
[29] N. Legrand, S. Raël, B. Knosp, M. Hinaje, P. Desprez, F. Lapicque, J. Power Sources 251 (2014) 370–378.
[30] F. Schomburg, B. Heidrich, S. Wennemar, R. Drees, T. Roth, M. Kurrat, H. Heimes, A. Jossen, M. Winter, J.Y. Cheong, F. Röder, Energ. Environ. Sci. 17 (2024) 2686–2733.
[31] British Standard Institution, (2019).
[32] G. Sordi, A. Rondi, D. Conti, A. Casalegno, C. Rabissi, Future Batter. 3 (2024) 100005.
[33] G. Sordi, M. Sedzik, A. Casalegno, C. Rabissi, Future Batter. 4 (2024) 100006.
[34] T. Beuse, M. Fingerle, C. Wagner, M. Winter, M. Börner, Batteries 7 (2021) 70.
[35] M.A. Cabañero, N. Boaretto, M. Röder, J. Müller, J. Kallo, A. Latz, J. Electrochem. Soc. 165 (2018) A847–A855.
[36] R. Amin, Y.-M. Chiang, J. Electrochem. Soc. 163 (2016) A1512–A1517.
[37] Z. Mao, M. Farkhondeh, M. Pritzker, M. Fowler, Z. Chen, J. Electrochem. Soc. 164 (2017) A39–A47.
[38] T. Liebmann, C. Heubner, M. Schneider, A. Michaelis, Mater. Today Energy 22 (2021) 100845.
[39] D. Andre, S.-J. Kim, P. Lamp, S.F. Lux, F. Maglia, O. Paschos, B. Stiaszny, J. Mater. Chem. A Mater. 3 (2015) 6709–6732.
[40] R. Gonçalves, S. Lanceros-Méndez, C.M. Costa, Electrochem. Commun. 135 (2022) 107210.
[41] J.S. Edge, S. O'Kane, R. Prosser, N.D. Kirkaldy, A.N. Patel, A. Hales, A. Ghosh, W. Ai, J. Chen, J. Yang, S. Li, M.-C. Pang, L. Bravo Diaz, A. Tomaszewska, M. W. Marzook, K.N. Radhakrishnan, H. Wang, Y. Patel, B. Wu, G.J. Offer, Phys. Chem. Chem. Phys. 23 (2021) 8200–8221.
[42] N. Hojat, P. Gentile, A.M. Ferreira, L. Šiller, J. Porous. Mater. 30 (2023) 93–101.
[43] N. Otsu, IEEE Trans. Syst. Man Cybern. 9 (1979) 62–66.
[44] C. Sha, J. Hou, H. Cui, J. Vis. Commun. Image Represent. 41 (2016) 339–351.
[45] B. Bozzini, P.L. Cavallotti, G. Giovanelli, Proc. R. Microscopical Soc. 31 (1996).
[46] D. Cui, J. Wang, A. Sun, H. Song, W. Wei, Scanning 2018 (2018) 2593780.
[47] B. Sekachev, N. Manovich, M. Zhiltsov, A. Zhavoronkov, D. Kalinin, B. Hoff, TOsmanov, D. Kruchinin, A. Zankevich, DmitriySidnev, M. Markelov, Johannes222, M. Chenuet, a-andre, telenachos, A. Melnikov, J. Kim, L. Ilouz, N. Glazov, Priya4607, R. Tehrani, S. Jeong, V. Skubriev, S. Yonekura,vugia truong, zliang7, lizhming, T. Truong, (2020).
[48] Y.-T. Chen, M. Duquesnoy, D.H.S. Tan, J.-M. Doux, H. Yang, G. Deysher, P. Ridley, A.A. Franco, Y.S. Meng, Z. Chen, ACS Energy Lett. 6 (2021) 1639–1648.
[49] S. Zhang, C.-X. Tong, X. Li, D. Sheng, Géotechnique 65 (2015) 911–922.
[50] M. Dupont, A.F. Hollenkamp, S.W. Donne, Electrochim. Acta 104 (2013) 140–147.
[51] J. Kim, S. Park, S. Hwang, W.-S. Yoon, J. Electrochem. Sci. Technol. 13 (2021) 19–31.
[52] S.D. Kang, W.C. Chueh, J. Electrochem. Soc. 168 (2021) 120504.
[53] O. Capron, R. Gopalakrishnan, J. Jaguemont, P. Van Den Bossche, N. Omar, J. Van Mierlo, Materials 11 (2018) 176.
[54] Z. Mao, M. Farkhondeh, M. Pritzker, M. Fowler, Z. Chen, Electrochim. Acta 222 (2016) 1741–1750.
[55] J. Landesfeind, D. Pritzl, H.A. Gasteiger, J. Electrochem. Soc. 164 (2017) A1773–A1783.
[56] C. Heubner, M. Schneider, A. Michaelis, J. Power Sources 288 (2015) 115–120.
[57] B.A. Boukamp, Electrochim. Acta 252 (2017) 154–163.
[58] S. Cruz-Manzo, P. Greenwood, J. Electroanal. Chem. 871 (2020) 114305.
[59] S. Barcellona, S. Colnago, L. Codecasa, L. Piegari, J. Energy Storage 73 (2023) 109202.
[60] M. Oldenburger, B. Bedürftig, A. Gruhle, F. Grimsmann, E. Richter, R. Findeisen, A. Hintennach, J. Energy Storage 21 (2019) 272–280.
[61] R.S. Negi, S.P. Culver, A. Mazilkin, T. Brezesinski, M.T. Elm, ACS Appl. Mater. Interfaces 12 (2020) 31392–31400.
[62] C. Tomon, S. Sarawutanukul, N. Phattharasupakun, S. Duangdangchote, P. Chomkhuntod, N. Joraleechanchai, P. Bunyanidhi, M. Sawangphruk, Commun. Chem. 5 (2022) 54.
[63] P. Iurilli, C. Brivio, V. Wood, J. Power Sources 505 (2021) 229860.
[64] D. Wu, H. Ren, Y. Guo, X. Zhang, Z. Zhang, J. Li, Ionics (Kiel) 25 (2019) 1595–1605.
[65] S.A. Watzele, L. Katzenmeier, J.P. Sabawa, B. Garlyyev, A.S. Bandarenka, Electrochim. Acta 391 (2021) 138969.
[66] X. You, M. Chaudhari, S. Rempe, L.R. Pratt, ECS Trans. 69 (2015) 107–111.
[67] J. Zhu, M. Knapp, X. Liu, P. Yan, H. Dai, X. Wei, H. Ehrenberg, IEEE Trans. Transp. Electrif. 7 (2021) 410–421.
[68] K. Xu, J. Electrochem. Soc. 154 (2007) A162.
[69] S. Käbitz, J.B. Gerschler, M. Ecker, Y. Yurdagel, B. Emmermacher, D. André, T. Mitsch, D.U. Sauer, J. Power Sources 239 (2013) 572–583.
[70] B.Y. Liaw, E.P. Roth, R.G. Jungst, G. Nagasubramanian, H.L. Case, D.H. Doughty, J. Power Sources 119–121 (2003) 874–886.
[71] T. Waldmann, J.B. Quinn, K. Richter, M. Kasper, A. Tost, A. Klein, M. Wohlfahrt-Mehrens, J. Electrochem. Soc. 164 (2017) A3154–A3162.
[72] V.A. Nikitina, Curr. Opin. Electrochem. 19 (2020) 71–77.
[73] P.M. Chekushkin, I.S. Merenkov, V.S. Smirnov, S.A. Kislenko, V.A. Nikitina, Electrochim. Acta 372 (2021) 137843.
[74] A.I. Komayko, E.E. Nazarov, O.A. Tyablikov, S.S. Fedotov, E.V. Antipov, V. A. Nikitina, J. Power Sources 624 (2024) 235589.
[75] C. Rojas, L. Oca, I. Lopetegi, U. Iraola, J. Carrasco, J. Energy Storage 80 (2024) 110384.
[76] L. Oca, E. Miguel, E. Agirrezabala, A. Herran, E. Gucciardi, L. Otaegui, E. Bekaert, A. Villaverde, U. Iraola, Electrochim. Acta 382 (2021) 138287.
[77] S. Sailer, M. Mundszinger, J. Martin, M. Mancini, M. Wohlfahrt-Mehrens, U. Kaiser, Micron 166 (2023) 103398.
[78] Z. Mao, M. Farkhondeh, M. Pritzker, M. Fowler, Z. Chen, M. Safari, J. Electrochem. Soc. 162 (2015) A716–A721.
[79] Z. Mao, M. Farkhondeh, M. Pritzker, M. Fowler, Z. Chen, J. Electrochem. Soc. 163 (2016) A458–A469.
[80] S. Jung, J. Power Sources 264 (2014) 184–194.